Remote Sensing Applications: Society and Environment 42 (2026) 101996

Contents lists available at ScienceDirect

Remote Sensing Applications: Society and Environment

journal homepage: www.elsevier.com/locate/rsase

Assessing spatial scale effects in multi-sensor fire fuel mapping in the heterogeneous landscapes of Tasmania ☆

Sophia Hoyer [a,b,*], Anke Fluhrer [a], Florian Hellwig [b,a], Steve Harwin [c], Jukka Matthias Krisp [b], Thomas Jagdhuber [a,b]

[a] *Microwaves and Radar Institute, German Aerospace Center (DLR), Oberpfaffenhofen, Germany*
[b] *Institute of Geography, Faculty of Applied Computer Science, University of Augsburg, Augsburg, Germany*
[c] *School of Geography, Planning, and Spatial Sciences, University of Tasmania, Hobart, Australia*

ARTICLE INFO

Keywords:
Fire fuel mapping
Object-based image analysis (OBIA)
Spatial scale effects
Random Forest
LiDAR
SAR
Sensor fusion

ABSTRACT

Effective fire-risk management in Tasmania requires vegetation maps that capture both broad fuel patterns and small, highly flammable gorse (*Ulex europaeus*) infestations. Yet gorse often occurs in fragmented patches that disappear in coarser land-cover products, raising uncertainty about how much fuel information is lost when regional maps are produced at moderate or coarse resolution. To clarify these scale effects we compare Object-Based Image Analysis-Random Forest fuel mapping at 0.5, 3 and 10 m in a heterogeneous Tasmanian agricultural landscape using fused optical, LiDAR and SAR features. Beyond accuracy at each scale, we quantify how classes merge, disappear, or persist between resolutions using transfer matrices and analyse how large a gorse patch must be to remain detectable at coarser scales. F1 scores are consistently high across scales (76%–99%), yet class-level behaviour differs substantially. The 3 m model achieves the highest gorse classification performance while maintaining geometric coherence of these shrub patches. When transferred from 0.5 m, 76% of fine-scale gorse area remains represented at 3 m, compared to only 36.8% at 10 m. Detection probability at 3 m increases monotonically with patch size, whereas at 10 m even large patches (10,000–30,000 m^2) are detected in only 60% of the cases. These results demonstrate that high within-scale accuracy does not guarantee cross-scale persistence of fine-grained fuels. 3 m resolution provides optimal scale–patch alignment for regional fuel-zone delineation in Tasmania, whereas sub-metre imagery is required for explicit identification of individual gorse infestations. Overall, the results confirm that spatial aggregation disproportionately affects narrow and fragmented vegetation types. Resolution choice is therefore not merely a technical setting, but a decisive factor in whether hazardous fine fuels remain visible in regional fuel assessments.

1. Introduction

In Australia, bushfires are a recurring and increasingly severe threat to both ecosystems and communities (Sharples et al., 2016). Although fire is a natural ecological process, recent decades have seen increasing frequency and intensity of extreme fire

---

☆ This work was supported in part by the European Space Agency (ESA), France through the provision of Planet SkySat imagery under the Third-Party Mission Data Sponsorship program, and in part by Planet Labs PBC through its Education and Research Program, which provided access to PlanetScope imagery under a research license.

* Corresponding author.
E-mail address: sophia.hoyer@dlr.de (S. Hoyer).

https://doi.org/10.1016/j.rsase.2026.101996
Received 15 December 2025; Received in revised form 27 February 2026; Accepted 23 March 2026

events, driven largely by climate change (Yu et al., 2020; Shi et al., 2021; Halgamuge et al., 2020). Effective fire management now depends on reliable vegetation maps that represent fuel structure and flammability, which guide prescribed burning, asset protection planning, and early-season hazard assessments (Taylor et al., 2024). A particular challenge in Tasmania is the management of *Ulex europaeus* (gorse), an invasive shrub that forms dense, highly flammable thickets. Even small, scattered gorse patches can act as unexpected fuel sources, influencing fire spread and suppression difficulty (Hartley et al., 2022; Anderson and Anderson, 2010). However, these patches are difficult to detect consistently across large areas because they are spatially fragmented and often spectrally similar to surrounding grasslands in medium-resolution satellite imagery (Hartley et al., 2022). Understanding how much gorse detail is retained (or lost) at different spatial resolutions is therefore essential for fire-risk mapping and regional fuel-load assessment (Arroyo et al., 2008). Unlike many agricultural regions where vegetation cover is relatively uniform, the Midlands of Tasmania form a highly heterogeneous mosaic of native grasslands, tussock patches, shrub corridors, woodland and small gorse infestations (Davidson et al., 2021). Vegetation structure can change over only a few metres, and grasslands alone span a wide range of heights and densities (Cowell et al., 2013). This fine-grained heterogeneity makes the region particularly sensitive to spatial resolution: classes that appear homogeneous in coarser agricultural landscapes are ecologically diverse here, and their patch boundaries directly influence fire behaviour (Taneja et al., 2021). Consequently, vegetation classification is not only meaningful but essential for capturing the functional diversity of grass- and shrub-dominated fuel types in this landscape.

Remote sensing offers scalable monitoring capabilities, with optical, LiDAR and SAR sensors capturing complementary information on vegetation composition, structure and surface roughness. Sub-metre imagery resolves fine-scale gorse structures but is expensive and spatially limited. Freely available missions such as Sentinel-1 and Sentinel-2 provide broad coverage, yet their spatial resolution often merges or obscures small shrub patches (Marcinkowska-Ochtyra et al., 2018; Plakman et al., 2020; Vizzari, 2022). Combining spectral, structural and textural features within an object-based image analysis (OBIA) framework improves classification by integrating spectral richness with contextual information (Gini et al., 2018; Mohammadpour et al., 2022; Dorigo et al., 2012), but the degree to which this mitigates scale-driven information loss remains little quantified. Previous studies have analysed scale effects using concepts such as minimum mapping unit (MMU) and minimum detectable patch size. Using synthetic binary patterns, Lechner et al. (2009) quantified how patch area, elongation and grid position control the probability of extracting small and linear features and showed that grid cells must be many times smaller than the feature width to achieve acceptable accuracy. Similar research studies have shown that coarse maps tend to underestimate the area and fragmentation of small patches or disturbances (Xin et al., 2013). Zhang et al. (2025) simulated scale aggregation effects and showed accuracy degradation with coarser resolution. While these studies provide important theoretical and simulation-based insights into scale effects, they primarily evaluate scale through controlled aggregation or single-resolution analyses. In contrast, our study examines how the same real-world vegetation patches persist or disappear across independently derived operational products at multiple spatial scales.

Additionally, it remains unclear how far fine-scale distinctions between gorse, grass communities and forest persist when maps are produced at coarser resolutions, or which sensor configurations retain enough class detail to remain operationally useful. Existing OBIA studies have explored segmentation scale (Hao et al., 2021) and multi-sensor fusion (Vizzari, 2022), but most assess each scale independently rather than examining how vegetation classes reconfigure across a nested 0.5–3–10 m gradient.

In this study, we extend the scale-effect analysis from comparing map-level accuracies to analysing patch-wise cross-scale detectability of invasive gorse fuel. Our patch-based cross-scale analysis moves beyond controlled aggregation experiments from earlier work (Lechner et al., 2009; Xin et al., 2013) by quantifying object-level retainment across independently segmented and classified products. It thereby links the minimum detectable patch size theory to operational multi-sensor fuel mapping. The study aims for explicit patch-size thresholds and scale-dependent recommendations for operational gorse and grass fuel mapping in heterogeneous agricultural landscapes. This leads to three guiding research questions:

1. How does the alignment between spatial resolution and vegetation-patch size affect the mapping of fire-relevant vegetation classes across 0.5, 3 and 10 m?
2. Which sensor or sensor combinations provide sufficient accuracy for fuel mapping in the heterogeneous landscapes of Tasmania?
3. How does gorse patch size influence cross-scale detectability and object persistence?

2. Study areas and database

The study areas are located in the Midlands of Tasmania and features agricultural land, gorse, diverse grassland communities, and small patches of trees. Three nested subsets (Fig. 1) were selected based on the presence of gorse, representativeness of agricultural landscapes, and data availability, covering 2.3 km^2 (SkySat), 23 km^2 (PlanetScope; PS), and 210 km^2 (Sentinel-1/-2), respectively. Table 1 summarises the datasets used in this study.

The airborne LiDAR was conducted by the company VirtualTas during a flight mission with the purpose of creating a digital twin of Tasmania. It was captured using a RIEGL VQ-1560i-DW sensor from an estimated flying height of approximately 700 metres above ground level, achieving a point density of approximately 38.65 points/m^2 (VirtualTAS, 2025). The LiDAR was recorded one year earlier (2024) than all other datasets, however, it was obtained during the same season (early autumn). To validate that no major vegetation changes occurred between the two acquisition dates, we visually inspected multi-temporal orthophotos from the Tasmanian LISTMap viewer for 2024 and 2025 (Department of Natural Resources and Environment Tasmania, 2025). We did not observe any temporal offsets that could affect CHM (Canopy Height Model)-based class discrimination. A SkySat collection was obtained through Planet Labs and European Space Agency (ESA) sponsorship, and downloaded as an ortho-analytical surface

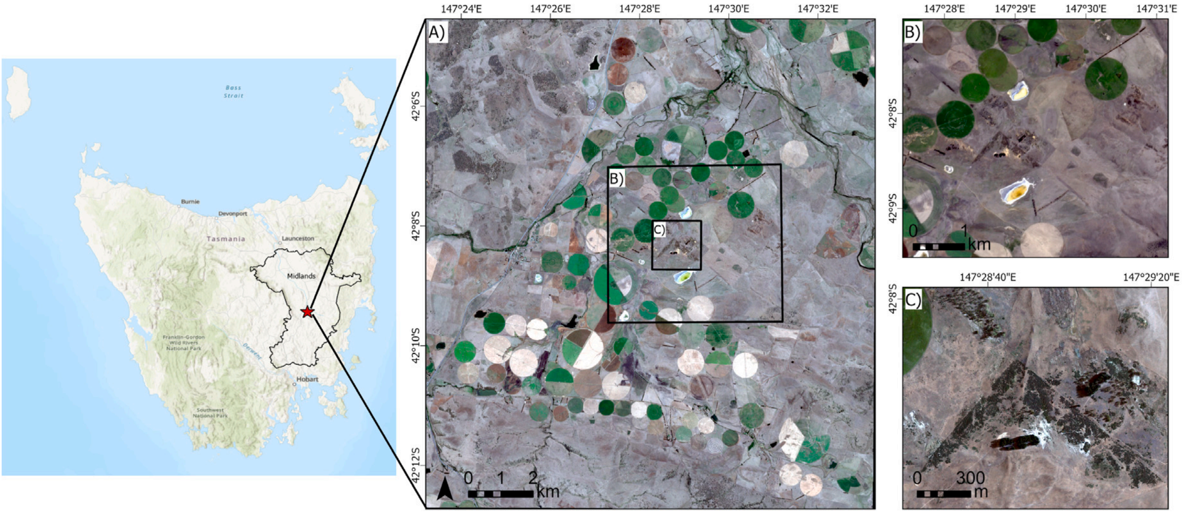

Fig. 1. Overview of the study areas in the Midlands of Tasmania. (A) shows the coarse area with 10 m Sentinel-2 as basemap. (B) presents the mid-scale area with 3 m PlanetScope imagery and (C) shows the fine-scale area with 0.5 m SkySat imagery.

Table 1
Overview of datasets employed in this study with their source, spatial and spectral resolutions, as well as recording dates.

Data	Source	Spatial Res.	Spectral Res.	Date
LiDAR	VirtualTAS	38.65 pnts/m^2	–	13/03/2024
SkySat	Planet	0.5 m	RGB+NIR	09/03/2025
PS	Planet	3 m	8-band	19/03/2025
S-1	Copernicus	10 m	VV+VH	03/03/2025
S-2	Copernicus	10 m	13-band	19/03/2025

Table 2
Spectral bands and their wavelengths in nm for Sentinel-2 [resolution in brackets], PlanetScope [3 m] and SkySat [0.5 m].

Spectral band	Sentinel-2	PlanetScope	SkySat
B01 (Aerosol)	443 (60 m)	431–452	–
B02 (Blue)	490 (10 m)	465–515	450–515
B03 (Green)	560 (10 m)	513–549	515–595
Green II	–	547–583	–
Yellow	–	600–620	–
B04 (Red)	665 (10 m)	650–680	605–695
B05 (Red edge)	705 (20 m)	697–713	–
B06 (Red edge)	740 (20 m)	–	–
B07 (Red edge)	783 (20 m)	–	–
B08 (NIR)	842 (10 m)	845–885	740–900
B8A (Narrow NIR)	865 (20 m)	–	–
B09 (Water vapour)	945 (60 m)	–	–
B10 (Cirrus)	1375 (60 m)	–	–
B11 (SWIR 1)	1610 (20 m)	–	–
B12 (SWIR 2)	2190 (20 m)	–	–

reflectance product via Planet Explorer. The image consists of four bands: red (R), green (G), blue (B), and near-infrared (NIR) (RGB+NIR). Some shadowing is visible in the image, cast from taller trees. The PS collection from the Super Dove sensor was obtained through a research license from Planet Labs. The image was harmonised by Planet Labs to fit Sentinel-2 (S-2) data. Lastly, the Sentinel-1 (S-1) and S-2 images were downloaded from the Copernicus Hub. All optical data have 0% cloud cover. Their band specifics are given in Table 2.

All imagery was projected to GDA2020/MGA Zone 55, resampled to a common resolution matching the analysis scale (0.5 m, 3 m, or 10 m) using the nearest neighbour interpolation method, and aligned using the Python package rasterio (v1.4.3) (Gillies and

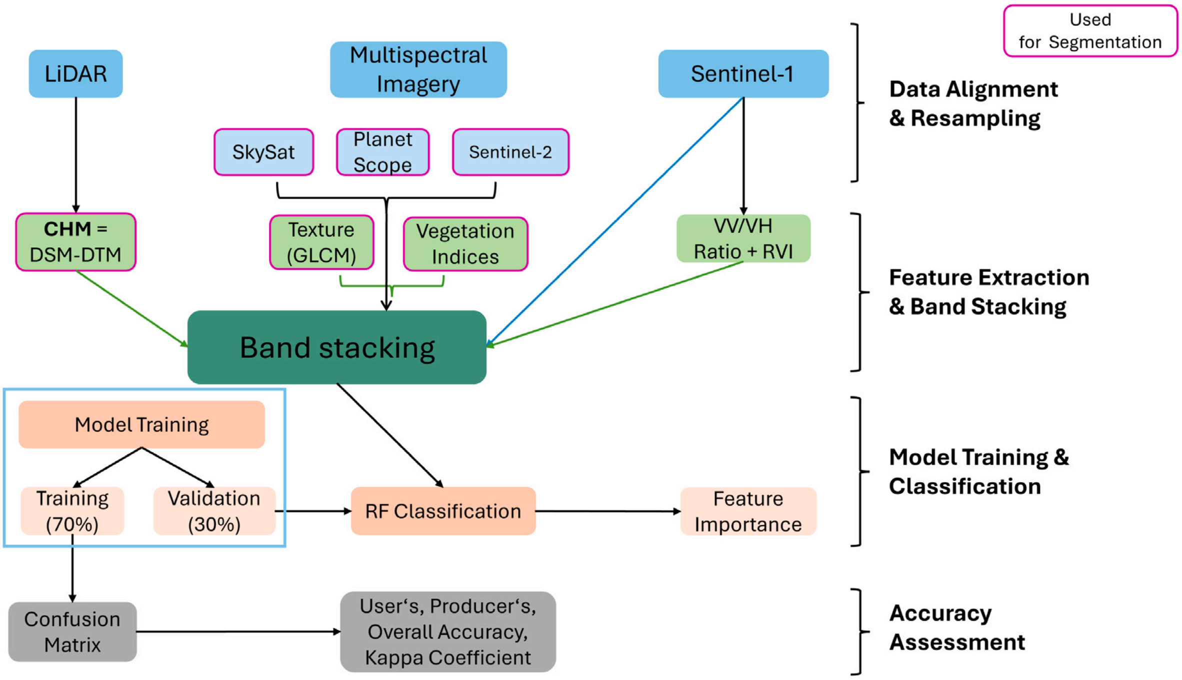

Fig. 2. Flowchart of the OBIA-RF approach for vegetation classification using LiDAR, multispectral, and SAR (S-1) imagery. CHM = Canopy Height Model, DSM = Digital Surface Model, DTM = Digital Terrain Model, GLCM = Grey Level Co-occurrence Matrix, RVI = Radar Vegetation Index.

contributors, 2024). The VirtualTas LiDAR was used to derive a Digital Elevation Model (DEM) and Digital Surface Model (DSM) at 0.5 m resolution to calculate a CHM.

S-1 pre-processing was done with ESA's Sentinel Application Platform (SNAP) software, including thermal noise removal, orbit, and terrain correction. For speckle filtering, the Block-Matching 3D (BM3D) algorithm was applied (Dabov et al., 2007).

3. Methodology

We applied an OBIA-Random Forest (RF) workflow at three spatial resolutions (0.5, 3 and 10 m), representing fine-scale gorse fuel units, functional type, and landscape-level mapping requirements. At each scale, we aligned multi-sensor data and extracted spectral, structural, and textural features to enable comparable RF classifications. As can be seen in Fig. 2 the workflow followed four steps: data alignment and resampling, feature extraction and band stacking, model training and classification, as well as an accuracy assessment. Each spatial scale was treated as an independent mapping scenario. Accordingly, segmentation, training data, classification and accuracy assessment were defined separately for each scale. This design reflects realistic fuel mapping rather than artificial model transfer in a controlled setting.

Table 3 outlines spectral band inputs and classification focus for each spatial scale. Previous studies have shown that sub-metre imagery is required to reliably detect tussock-form grasses (Pham et al., 2024; Ogliari et al., 2023). On this basis, we mapped characteristic tussock-form grass structures (*Lomandra longifolia*) at 0.5 m resolution (fine-scale), where the detail was sufficient to separate it from other native grass communities. At coarser scales (3 m, 10 m), such species-level distinctions were no longer spectrally or structurally separable and were therefore aggregated into the broader class ‘grass communities’. These class groupings reflect the ecological reality that species-level distinctions are detectable only at sub-metre scale, while broader vegetation functional types dominate the spectral signatures at medium and coarse resolutions. However, with a coarser resolution, the area that can be classified increases as the computational load decreases. Therefore, the two coarser areas are ten (23 km^2) and 100 (210 km^2) times the core fine-scale area. Accuracy and feature importance are interpreted within each scale only and are not directly compared across spatial extents and scales. Cross-scale comparisons are based solely on the overlapping fine scale area.

By analysing the classification performance and feature importance per scale, this study aims to quantify which sensor types provide the most value for detecting fine gorse fuel units at varying spatial extents. After that, it is tested whether the fine-scale approach can be interpreted as a useable signal for coarser and more cost-efficient gorse zone maps.

Table 3
Spatial scales and their inputs/focus for vegetation classification.

Scale	Purpose	Data inputs	Classification focus	Area (km^2)
0.5 m	Fine-fuel detail	SkySat+CHM	Individual gorse, tussock patterns	2.3
3 m	Fuel-zone mapping	PS+S1+S2	Gorse-grass patch clusters	23
10 m	Landscape context	S1+S2	Broad gorse/open/forest zones	210

Table 4
Vegetation indices used in the analysis.

Index	Equation	Reference
NDVI	$\frac{NIR-Red}{NIR+Red}$	Rouse et al. (1974)
EVI	$\frac{2.5\cdot(NIR-Red)}{NIR+6\cdot Red-7.5\cdot Blue+1}$	Zeng et al. (2022)
SAVI	$\frac{(1+L)(NIR-Red)}{NIR+Red+L}$	Huete (1988)
NDWI	$\frac{Green-NIR}{Green+NIR}$	McFeeters (1996)
RVI	$\frac{4\cdot\sigma^{VH}}{\sigma^{VV}+\sigma^{VH}}$	Kim and van Zyl (2004)

3.1. Feature extraction

To improve classification accuracy, we derived spectral, structural and textural features from the optical, radar and LiDAR datasets. From the optical imagery, we computed four vegetation indices: the Normalised Difference Vegetation Index (NDVI), Enhanced Vegetation Index (EVI), Soil-Adjusted Vegetation Index (SAVI) and Normalised Difference Water Index (NDWI) following Xue and Su (2017) (see Table 4). For Sentinel-1, the Radar Vegetation Index (RVI) was calculated using the dual-polarisation adaptation based on $\sigma^0_{VV} \approx \sigma^0_{HH}$ (Kim and van Zyl, 2004; Trudel et al., 2012; Holtgrave et al., 2020), where σ^0 denotes the backscatter coefficient (Richards, 2005).

Textural information was added using grey level co-occurrence matrix (GLCM) features, which have been shown to improve vegetation mapping (Mohammadpour et al., 2022; Agüera et al., 2008; Feng et al., 2015). Following Hall-Beyer (2017), we retained four largely non-redundant measures: contrast, mean, homogeneity and entropy. Textures were derived from the first principal component of each optical dataset using standard settings (distance = 1, 64 grey levels). Structural information was incorporated at the fine spatial scale using the LiDAR-derived canopy height model.

3.2. Image segmentation

We used multi-resolution segmentation (MRS) in eCognition (Trimble Inc., 2026), a commonly applied algorithm for generating homogeneous objects in high-resolution imagery (Meinel and Neubert, 2004; Baatz and Schäpe, 2000). Segmentation parameters were tuned iteratively to reflect vegetation structure at each scale.

For each area, the highest resolution multispectral bands per scale, the NDVI, and the textural bands were included in the MRS. For the fine-scale region, the CHM was included as well and weighted with a factor of three to single out trees and gorse patches (Table 9 in the Appendix). Other input layers were only weighted once. The parameter settings differed between scales to reflect structural characteristics of the vegetation patches and scale. Scale parameters were adjusted iteratively by visual inspection.

3.3. Classification

OBIA was used to reduce pixel-level noise and to improve class discrimination compared with conventional pixel-based approaches (Niemeyer et al., 2008; Hussain et al., 2013; Kavzoglu and Tonbul, 2018). OBIA allows spectral, structural and ancillary information to be combined at the segment level, which supports vegetation mapping across different spatial resolutions. As a classification algorithm, RF was selected for its robustness to mixed data types and limited training samples. In OBIA, RF efficiently integrates multispectral, LiDAR, and radar features and requires minimal parameter tuning compared to alternative algorithms such as Support Vector Machines (Breiman, 2001; Bialas et al., 2019). RF models were implemented in Python using scikit-learn with 200 trees, class-balanced weights and out-of-bag error estimation enabled (scikit-learn developers, 2023).

A separate RF model was trained for each spatial scale. Each model was based on the highest-resolution base sensor available (SkySat for fine-scale, PS for mid-scale, and Sentinel-2 for coarse-scale) and used scale-specific training data and features. This approach reflects realistic data availability at each mapping scale. The goal was not to transfer one model across scales, but to quantify how vegetation-class definitions change when segmentation and resolution differ. In this way, any differences in classification performance reflect realistic scale-dependent mapping conditions. Training objects were assigned based on dominant vegetation and ambiguous cases were excluded. The classes included are grass communities, trees, gorse, bare land, agricultural land, and water for mid- and coarse-scales (see Table 5). At the fine-scale Lomandra was additional classified. Water polygons were underrepresented in the study area, resulting in fewer training and test segments than for other classes and hence, are completely omitted in the fine-scale area. The final number of labelled objects can be seen in Table 5. Training and testing areas

Table 5
Training and testing segment counts per class and scale. Values are shown as `train/test`, with the last column giving the total values.

Scale	Lomandra	Grass Comm.	Trees	Gorse	Bare land	Agricultural land	Water	Total
Fine	52/16	50/13	42/16	48/18	54/16	22/9	–	268/88
Mid	–	44/14	35/12	32/13	44/16	43/17	7/4	205/76
Coarse	–	32/14	42/21	38/18	44/12	44/14	12/5	212/70

were geographically separated to ensure spatial independence and reduce spatial autocorrelation bias. The areas differ in their extent to cover the entire study region per scale and to train the RF in perspective of their resolution.

Features were extracted for each segment across all input layers (spectral bands, vegetation indices, texture bands, CHM, and SAR where available). For each segment per band, the mean, min, max, range, and standard deviation were computed. In addition, chromaticity features were calculated. Geometric descriptors included object area, perimeter, and shape index.

Each scale was analysed independently using its native sensor combination, but the classification parameters (number of trees, mtry) and accuracy metrics were standardised to enable direct cross-scale comparison.

To evaluate the contribution of each sensor and feature type, separate RF models were trained for each resolution, including variants with VIs, texture metrics and the CHM. Feature importance scores were extracted to identify variables contributing most to class discrimination (Menze et al., 2009; Breiman, 2001). Classification accuracy was assessed using spatially independent test objects. From the confusion matrices we derived overall accuracy (OA), user's (UA) and producer's accuracies (PA), kappa, and per-class F1-scores (Stehman and Foody, 2019; Congalton and Green, 2008). The 0.5 m, 3 m and 10 m classifications were generated independently. No map was resampled or aggregated from another scale prior to comparison.

3.4. Cross-scale analysis

To be able to investigate map level consistency and quantify thematic overlap, we calculated area-transfer matrices between fine-, mid- and coarse-scale outputs. We report forward recall (fine-to-coarse agreement), backward precision (coarse-to-fine agreement) and their symmetric overlap using the Dice coefficient, commonly applied polygon-level accuracy measure for object-based classifications (Guindon and Zhang, 2017). To account for minor geometric offsets related to co-registration or segmentation boundaries, all overlap metrics were additionally computed using buffered fine-scale objects (3 m for mid-scale comparisons and 10 m for coarse-scale comparisons). These buffer widths match the target resolutions and provide a robustness check for boundary-related uncertainties, as it was recommended by Tyukavina et al. (2025). Next to the map comparison, we also quantify the retainment of the gorse patches between scales. We therefore cover both directional views of object class disappearance. Whole map comparison (top down) and individual patch (bottom up) analysis. For this, we derived the gorse areas from the 0.5 m segmentation by dissolving gorse-classified segments into contiguous polygons. These geometries served as the reference representation of gorse distribution at fine spatial resolution. To assess cross-scale detectability, the independently classified maps at 3 m and 10 m resolution were spatially intersected with the reference layer. A reference patch was considered retained at a coarser scale if the gorse classified segment overlapped its geometry by more than 50%. Patches without any gorse overlap were classified as undetected. Patch retainment was quantified per patch-size class. The 50% criterion reflects a majority-area definition of patch survival, consistent with dominant class assignment in object-based mapping (Blaschke, 2010).

4. Results

The results are presented in three parts. First, we summarise within scale performance and the achieved accuracies per scale. Second, we report the transfer matrices and thematic overlap of the classified maps. Third, we assess the gorse detectability across scales.

4.1. Within scale performance

Fig. 3 shows the segmentation results across all scales over the same area. At fine-scale, the gorse patch is over-segmented. Thus, small tussock grass clumps appear as separate objects. Mid-scale segmentation captures the structure more clearly, with trees grouped into single objects. At coarse-scale, the area is under-segmented and differences between gorse and scattered trees are barely visible in the S-2 RGB. Within a common 1 km^2 grid (Fig. 3), segmentation produced 2126 objects at fine scale, 117 at mid scale, and 52 at coarse scale. The high number at fine-scale reflects deliberately over-segmentation to capture small tussock grass clumps. Mid-scale segmentation produced spatially coherent vegetation units that aligned with the 3 m sensor resolution.

Across all three resolutions, the RF models achieved high overall accuracies, particularly at fine and mid scales (Fig. 4).

Tables 10, 11, and 12 in the Appendix report UA and PA for each class, together with confidence intervals and kappa statistics for the best-performing model at each scale. Confidence intervals are generally tight for user's accuracies but widen for producer's accuracies in spatially fragmented vegetation classes, particularly gorse at the coarse scale. A feature importance analysis for each scale is provided in the Appendix (Fig. 7) as well. These rankings show that structural height dominates at fine scale, while optical

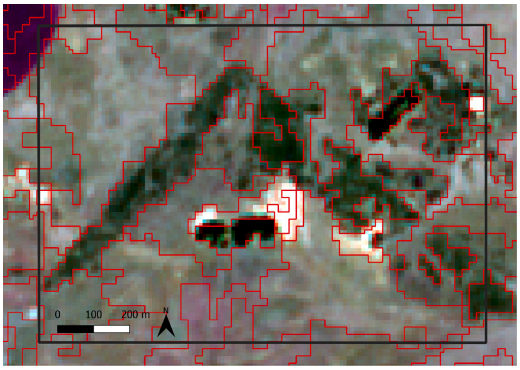

(a) Segmentation of 52 objects based on S-2 bands, texture, and S-2 based NDVI.

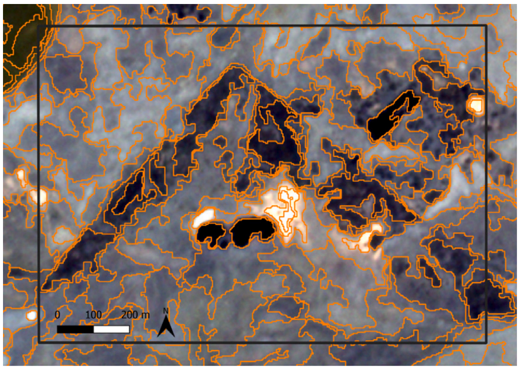

(b) Segmentation of 117 objects based on PS-bands, texture, and PS-based NDVI.

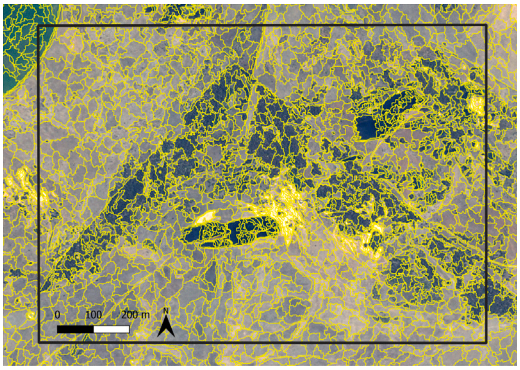

(c) Segmentation of 2126 objects based on SkySat bands, texture, SkySat based NDVI, and CHM.

Fig. 3. Segmentation results for 1 km^2 for the (a) coarse-scale, (b) mid-scale, and (c) fine-scale resolution levels (see Table 3).

NIR and vegetation index bands drive separability at mid and coarse resolution, consistent with the scale-dependent performance patterns described above.

Fig. 4 integrates OA and F1 across all sensor configurations and scales of the three relevant classes. Fine- and mid-scale models cluster tightly at high performance levels, with OA exceeding 90% and F1 values above 85%. Coarse-scale models exhibit greater variability, with only the most feature-rich configurations approaching the accuracy of finer resolutions. This spread highlights the stronger dependence of 10 m OBIA classification on sensor choice and feature design. Contrary to initial expectations, the mid scale provides the single most reliable configuration overall: S-2+VI achieves the highest combined OA and F1 for gorse, forest and grass communities when based on a 3 m segmentation. At fine scale, the SkySat+VI+CHM+texture (Full Stack) stack performs best but

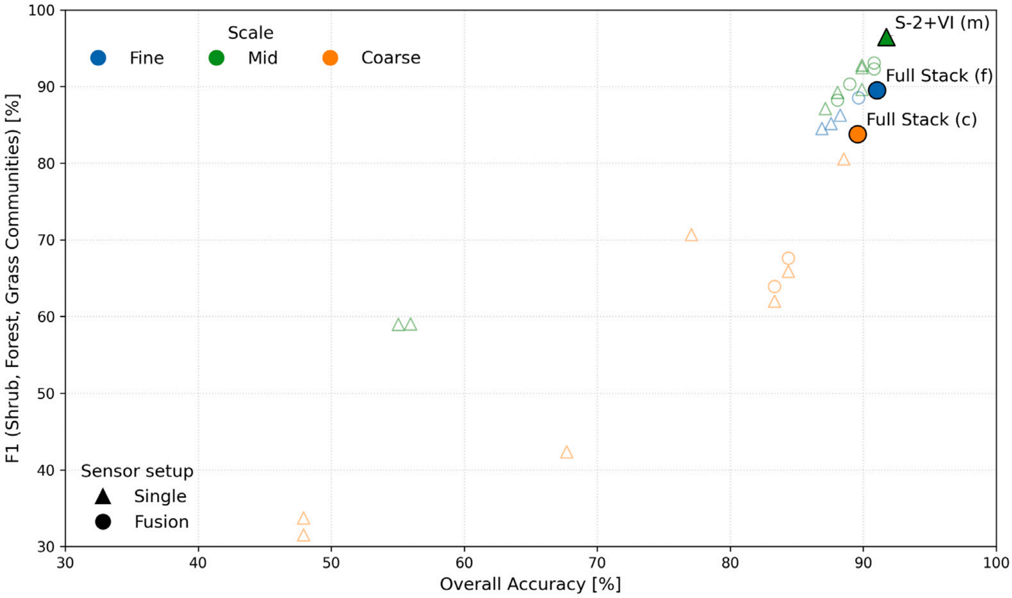

Fig. 4. Overall accuracy (OA) versus F1 for gorse, forest and grass communities across all sensor configurations and scales. Colour indicates scale; shape indicates sensor setup. Filled markers highlight the most reliable configuration at each scale.

does not surpass the top mid-scale setup. At coarse scale, the S-1+S-2+VI+texture (Full Stack) combination is strongest, achieving F1 values above 83%, but simpler configurations fall far below, underscoring the need for extensive feature augmentation at coarse resolution.

4.2. Cross-scale classification overlap

Table 6 reports three complementary measures: forward recall (how much of each fine-scale class is retained in the coarser category), backward precision (how pure the coarse objects are when viewed at finer detail), and the Dice coefficient as a symmetric indicator of overlap. Buffered variants (3 m for mid-scale, 10 m for coarse-scale) were also tested to reduce boundary effects. The Dice coefficient balances both perspectives. Results show that classes gorse and forest maintain good correspondence at the mid-scale, but their consistency drops at coarse resolution, especially in terms of backward precision. Gorse and the herbaceous classes decline sharply in both recall and Dice when aggregated to coarse-scale, confirming their sensitivity to object size and spatial context. The buffered variants reveal that boundary effects only partly explain the inconsistencies. For stable classes like agriculture or forest, buffered and non-buffered values are nearly identical, confirming that their spatial patterns are robust to edge effects. In contrast, gorse, grass, and especially Lomandra show much higher gains in backward precision when buffered, indicating that much of their apparent inconsistency comes from thin, fragmented patches being reassigned at segment boundaries. The stronger shifts in backward precision compared to forward recall arise because coarse segments are much larger than fine-scale patches, meaning boundary pixels make up a bigger share of each coarse unit and disproportionately affect how pure those aggregated segments appear once edges are excluded.

4.3. Gorse patch detectability

To get an impression of the size of individual gorse patches, Table 7 shows the statistical description. The median patch size is 380 m^2, while the mean patch is 1900 m^2, indicating a strongly right-skewed distribution dominated by small patches.

Fig. 5 shows the detectability of gorse patches depending on their size. Detection probability increases with patch size at 3 m sensor resolution, reaching 100% for the largest patches. In contrast, the 10 m classification retains only 60% of the largest patches and shows no consistent monotonic size response pattern.

Fig. 6 visualises the detected gorse patches in the fine scale area. The large round patches are detected by both. Smaller patches may be retained when spatially adjacent to larger gorse objects, reflecting aggregation effects at coarser resolution. The linear long delineated patches on the right hand side were detected by 3 m, however not by 10 m, despite having a similar area size to the rounder patches on the left. Both classification failed to detect fragmented smaller (<100 m^2) gorse patches.

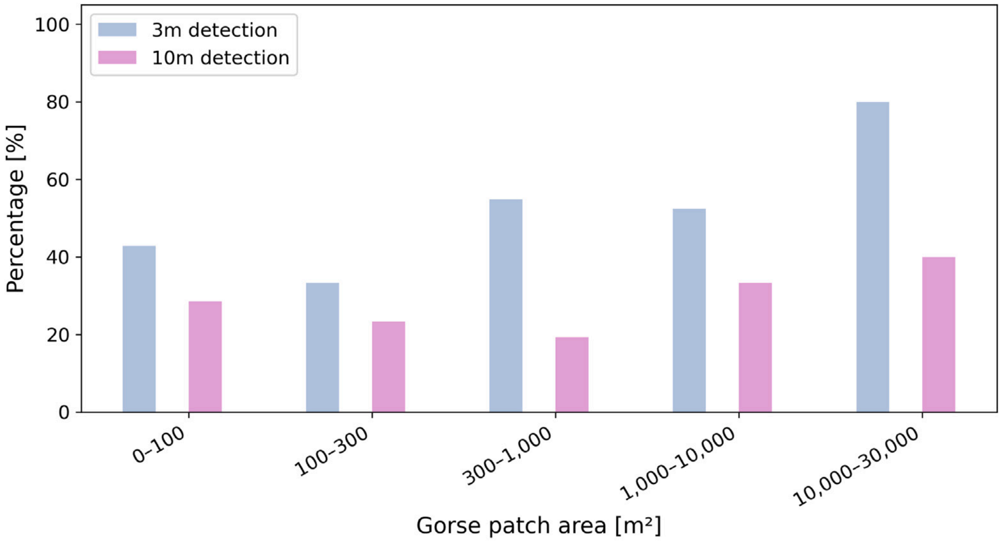

Fig. 5. Size-dependent detectability of reference gorse patches. Bars indicate the proportion (%) of 0.5 m reference patches within each area class that were overlapped by at least 50% by a gorse segment in the 3 m and 10 m classifications.

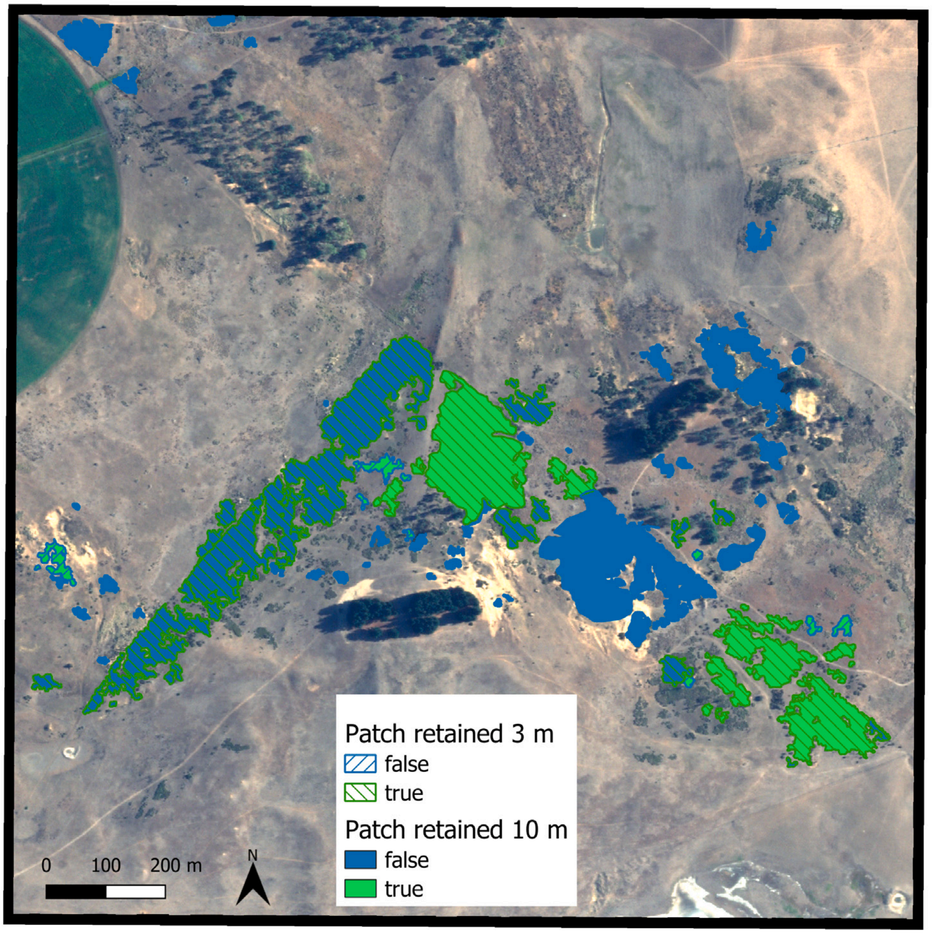

Fig. 6. Map shows the detection of gorse patches at 3 and 10 m in the fine scale area.

Table 6
Cross-scale consistency metrics. Forward = fine→scale recall, Backward = scale→fine precision, Dice = symmetric overlap (F1). Buffered values in brackets; 3 m for mid-scale, 10 m for coarse-scale.

Class	Scale	Forward recall	Backward precision	Dice
Gorse	Mid	0.76 (0.73)	0.55 (0.76)	0.63 (0.75)
	Coarse	0.37 (0.35)	0.32 (0.75)	0.34 (0.48)
Forest	Mid	0.76 (0.75)	0.56 (0.92)	0.64 (0.83)
	Coarse	0.82 (0.81)	0.26 (0.81)	0.39 (0.81)
Bare land	Mid	0.49 (0.49)	0.50 (0.68)	0.49 (0.57)
	Coarse	0.71 (0.71)	0.55 (0.92)	0.62 (0.82)
Lomandra	Mid	0.33 (0.32)	0.09 (0.13)	0.14 (0.18)
	Coarse	0.07 (0.06)	0.10 (0.22)	0.08 (0.09)
Grass Comm.	Mid	0.46 (0.45)	0.40 (0.53)	0.43 (0.49)
	Coarse	0.05 (0.05)	0.25 (0.51)	0.09 (0.09)
Agriculture	Mid	0.98 (0.98)	0.77 (0.94)	0.86 (0.96)
	Coarse	0.97 (0.97)	0.65 (0.97)	0.78 (0.97)

Table 7
The size of gorse patches in the small scale area.

Statistics	Size (in m^2)
Count	101
Min	23.01
Median	379.80
Mean	1900.03
Std	4974.83
Max	29,433.47

5. Discussion

5.1. Scale-patch alignment and sensor contribution

Detecting small, highly flammable gorse patches is critical for fire-risk assessment because these patches act as fine-fuel ignition points and can accelerate fire spread in agricultural landscapes (Anderson and Anderson, 2010). Whether such hazardous fuels remain visible in mapped products depends strongly on how well spatial resolution matches vegetation-patch size. Among the three resolutions, 3 m provided the most coherent representation of gorse–grass structure at the regional fuel-zone scale. At this scale, segmentation units approximated the typical extent of gorse clusters, producing stable objects that preserved fuel geometry and yielded the highest class separability. This confirms that classification performs best when mapping units align with the ecological scale of vegetation patches (Blaschke, 2010; Hao et al., 2021). At 0.5 m, gorse could be mapped as a distinct class, but segmentation subdivided continuous patches into numerous small objects, increasing internal heterogeneity. Fine-scale imagery is therefore optimal for detecting individual gorse plants, yet less effective for representing broader fuel continuity. At 10 m, gorse and grass formations frequently fell below the MMU and were aggregated into broad mixed segments, even when multi-sensor inputs were used. Although broader vegetation types remained distinguishable, the finer spatial structures that determine connected fuel pathways were no longer resolved (Sá et al., 2022; Macintyre et al., 2020). In summary, the results indicate that spatial resolution determines which ecological property is preserved: sub-metre imagery maximises object-level precision, whereas 3 m provides the most operationally coherent representation of fuel zones. Resolution choice must therefore reflect whether management aims at identifying discrete ignition sources or mapping continuous fuel patterns across landscapes.

When examining sensor contribution, scale-dependent patterns emerge. Across all resolutions, optical spectral information formed the basis of vegetation discrimination. At 0.5 m, however, structural information was decisive: while SkySat bands provided spectral contrast, the CHM contributed most to separating gorse from taller vegetation. At 3 m and 10 m, the relative contribution of sensor domains shifted as spatial detail decreased. Radar information supported discrimination at 3 m where structural patterns were still partially resolved. At 10 m, optical texture and VIs became relatively more influential, yet neither radar nor texture could compensate for geometric information lost through spatial aggregation. Once the patch structure falls below the mapping unit, no additional sensor restores it.

5.2. Cross-scale consistency

Fire-risk assessment frequently relies on vegetation maps produced at multiple spatial resolutions. However, interpreting maps across resolutions is challenging because class boundaries and class definitions do not necessarily persist when imagery is aggregated to coarser scales. For species like gorse (small, patchy) such scale-dependent loss of detail has direct consequences for fuel assessments. Our results show that high within-scale accuracy does not guarantee cross-scale persistence of vegetation objects. Broad and spatially homogeneous classes (e.g., agriculture) remain largely stable when aggregated from 0.5 to 10 m (Table 6). In contrast, narrow and fragmented vegetation types exhibit systematic instability. The transfer matrices confirm that this loss of spatial identity is systematic.

Buffered metrics help distinguish boundary artefacts from true scale effects. Backward precision is especially sensitive to segment size: large coarse-scale segments inevitably span multiple fine-scale classes, and boundary removal disproportionately increases their internal purity. The observed changes (mean $\Delta = 0.01$ for forward recall vs. 0.26 for backward precision) with buffering indicate that only part of the inconsistency arises from boundary misalignments; the rest reflects genuine scale-driven aggregation.

This pattern is consistent with the Modifiable Areal Unit Problem (MAUP Openshaw, 1984), whereby aggregation into larger spatial units alters thematic representation. Josselin and Louvet (2019) showed that GEOBIA-derived shape and texture metrics vary systematically with segmentation scale, demonstrating that OBIA is not immune to MAUP. Our transfer-matrix approach extends this insight to thematic class behaviour, quantifying how objects change their class as they are aggregated. As with any classification-based consistency analysis, residual errors contribute to observed discrepancies. For example, the coarse gorse class achieved an F1-score of 76%, placing an upper limit on detectable consistency. Additionally, each resolution was classified independently, meaning sensor differences may also contribute to spatial differences. Thus, our results exhibit MAUP-like behaviour rather than representing a pure test of MAUP consistency. Nevertheless, the coherent spatial patterns (stability in broad classes and systematic dissolution of patchy ones) strongly indicate that the main driver of cross-scale inconsistency is segmentation-driven aggregation, not random error.

5.3. Patch-level persistence

While the transfer matrices quantify changes in the mapping and thematic changes, they do not answer how large a gorse patch has to be detected by coarser resolutions. The patch-level detectability analysis shows that scale effects act directly on individual objects. At 3 m resolution, detection probability clearly increases with patch size. At 10 m, however, even relatively large gorse patches are not reliably retained (see Fig. 5). Linear corridors and narrow structures disappear more often once their width approaches the effective mapping unit (see Fig. 6). This pattern is consistent with the findings of Lechner et al. (2009), who showed that the probability of extracting linear features decreases when grid cells become similar in size to the feature width. The 10 m classification was not able to detect the linear gorse patches despite having a larger overall area, but managed to retain the oval shaped patches. In such situations, objects are not simplified, they are absorbed into neighbouring dominant classes. Similar scale-related effects have been reported in other fragmented ecosystems. For example, Zhang et al. (2025) observed systematic area underestimation and declining accuracy when ultra-high resolution mangrove maps were aggregated to coarser resolutions, especially in habitats composed of narrow and discontinuous patches. Our results show that comparable geometric constraints apply to fire-prone gorse systems.

Importantly, gorse patches can even disappear when inter accuracies remains high. This suggests that global metrics such as OA mask ecological information loss. In this case, the effect is not just a gradual reduction in mapped area, but the complete loss of individual objects. From a fire-management perspective, this distinction is critical. While 3 m products retain most spatial gorse structures, 10 m maps primarily indicate general shrub zones and cannot reliably represent fine-scale fuel patterns.

Overall, the results confirm that spatial aggregation disproportionately affects narrow and fragmented vegetation types. Resolution choice is therefore not merely a technical setting, but a decisive factor in whether hazardous fine fuels remain visible in regional fuel assessments.

6. Conclusion

Fuel-oriented vegetation mapping in Tasmania must balance the representation of broad fuel zones with the detection of small, highly flammable gorse patches that can drive local fire spread. By comparing independently derived OBIA–Random Forest classifications at 0.5, 3 and 10 m, this study moved beyond within-scale accuracy assessment to explicitly quantify cross-scale class persistence and patch-level survival. Despite high accuracies within each resolution (76–99%), cross-scale analyses revealed that vegetation products are not interchangeable. Using area-weighted transfer matrices and patch detectability analysis, we showed how fine-scale gorse patches are progressively reduced, absorbed, or retained as mapping units increase. While broad and homogeneous classes remained relatively stable, fragmented gorse fuels exhibited strong scale dependence.

Among the tested resolutions, 3 m provided the most robust alignment between mapping unit and vegetation-patch structure, preserving most fine-scale gorse area and showing stable size-dependent detectability. Sub-metre data were required for explicit mapping of individual gorse infestations, whereas 10 m products primarily represented aggregated shrub zones rather than discrete fuel sources. These results demonstrate that high within-scale accuracy does not guarantee cross-scale persistence of fine-grained fuels. The presented cross-scale detection framework provides practical, scale-aware guidance for selecting appropriate spatial resolutions in fuel-load assessment, bushfire-risk modelling, and early detection of invasive gorse hazards in Tasmania.

CRediT authorship contribution statement

Sophia Hoyer: Writing – original draft, Visualization, Validation, Software, Methodology, Investigation, Funding acquisition, Formal analysis, Data curation, Conceptualization. **Anke Fluhrer:** Writing – review & editing, Visualization, Supervision, Resources, Methodology, Data curation. **Florian Hellwig:** Writing – review & editing. **Steve Harwin:** Writing – review & editing, Supervision, Resources, Methodology, Data curation, Conceptualization. **Jukka Matthias Krisp:** Writing – review & editing, Supervision, Project administration. **Thomas Jagdhuber:** Writing – review & editing, Supervision, Project administration.

Table 8
GLCM texture features used in the analysis.

GLCM	Equation	Type
Mean	$\sum_{i,j=0}^{N-1} i\, P_{ij}$	Statistics group
Contrast	$\sum_{i,j=0}^{N-1} P_{ij}(i-j)^2$	Contrast group
Homogeneity	$\sum_{i,j=0}^{N-1} \frac{P_{ij}}{1+(i-j)^2}$	Contrast group
Entropy	$\sum_{i,j=0}^{N-1} P_{ij}\left[-\ln(P_{ij})\right]$	Orderliness group

Table 9
Segmentation parameters and input layers used at each scale.

Scale level	Scale	Shape	Compac.	Inputs
Fine	100	0.5	0.9	SkySat, CHM, GLCM, NDVI
Mid	100	0.1	0.9	PS, GLCM, NDVI
Coarse	80	0.6	0.8	S-2, GLCM, NDVI

Table 10
Per-class accuracy metrics with 95% confidence intervals (CI) of full stack fine-scale model.

Class	UA	PA	F1	UA CI	PA CI	F1 CI
Gorse	0.96	0.85	0.90	[0.89, 1.00]	[0.73, 0.97]	[0.82, 0.97]
Agricultural land	1.00	1.00	1.00	[1.00, 1.00]	[1.00, 1.00]	[1.00, 1.00]
Bare land	1.00	1.00	1.00	[1.00, 1.00]	[1.00, 1.00]	[1.00, 1.00]
Tree	0.90	0.95	0.93	[0.82, 0.97]	[0.87, 1.00]	[0.86, 0.97]
Grass communities	0.90	0.95	0.92	[0.79, 1.00]	[0.84, 1.00]	[0.84, 1.00]
Lomandra	0.79	0.81	0.79	[0.65, 0.93]	[0.65, 0.97]	[0.67, 0.90]
Overall accuracy	0.91			[0.88, 0.96]		
Kappa	0.89			[0.83, 0.94]		

Ethics in publishing statement

All authors agree that:

This research presents an accurate account of the work performed, all data presented are accurate and methodologies detailed enough to permit others to replicate the work.

This manuscript represents entirely original works and or if work and/or words of others have been used, that this has been appropriately cited or quoted and permission has been obtained where necessary.

This material has not been published in whole or in part elsewhere.

The manuscript is not currently being considered for publication in another journal.

All authors have been personally and actively involved in substantive work leading to the manuscript and will hold themselves jointly and individually responsible for its content.

Declaration of Generative AI and AI-assisted technologies in the writing process

That generative AI and AI-assisted technologies have not been utilised in the writing process or if used, disclosed in the manuscript the use of AI and AI-assisted technologies and a statement will appear in the published work.

That generative AI and AI-assisted technologies have not been used to create or alter images unless specifically used as part of the research design where such use must be described in a reproducible manner in the methods section.

Declaration of competing interest

The authors declare that they have no known competing financial interests or personal relationships that could have appeared to influence the work reported in this paper.

Acknowledgments

The authors are very grateful to Dr. Michael Wurm and Manuel Köberl (DLR - German Aerospace Center, German Remote Sensing Data Center) for providing access to the eCognition software.

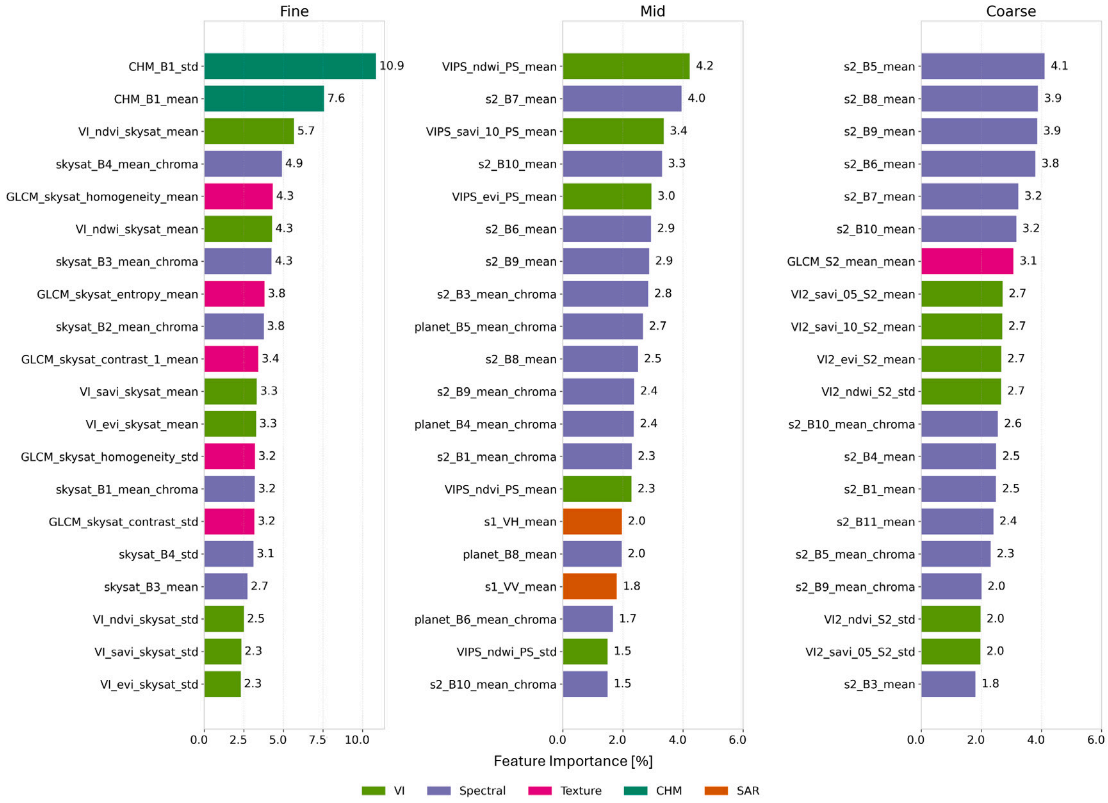

Fig. 7. Feature importance for all full stack runs per scale. Shown are only the top 20 bands for each scale.

Table 11
Per-class accuracy metrics with 95% confidence intervals (CI) of S-2+VI mid-scale model.

Class	UA	PA	F1	UA CI	PA CI	F1 CI
Gorse	1.00	1.00	1.00	[1.00, 1.00]	[1.00, 1.00]	[1.00, 1.00]
Agricultural land	0.88	1.00	0.94	[0.79, 0.97]	[1.00, 1.00]	[0.88, 0.98]
Bare land	0.91	0.84	0.87	[0.84, 1.00]	[0.68, 0.96]	[0.77, 0.96]
Water	1.00	0.25	0.40	[1.00, 1.00]	[0.00, 0.75]	[0.40, 0.86]
Forest	1.00	1.00	1.00	[1.00, 1.00]	[1.00, 1.00]	[1.00, 1.00]
Grass communities	0.87	0.91	0.89	[0.76, 1.00]	[0.74, 1.00]	[0.80, 0.96]
Overall accuracy	0.91			[0.82, 0.96]		
Kappa	0.85			[0.84, 0.94]		

Appendix

Table 8 list the GLCM equations and Table 9 gives the eCognition input parameters for the segmentation tasks for each scale. Tables 10, 11, 12 give the 95% confidence intervals with UA and PA of the best scored models for each scale along with kappa statistics and OA scores. Fig. 7 shows the feature importance analysis of the full stack model configurations across all scales. Fig. 8 compares the best result maps for all three investigated resolutions (all features combined for fine- and coarse-scale and S-2+VI for mid-scale). Gorse patches delineated at fine-scale (0.5 m) (Panel C) reappear at mid-scale as continuous shrub objects and at coarse-scale as broader shrub zones (Panels B-A).

Data availability

Data will be made available on request.

Table 12
Per-class accuracy metrics with 95% confidence intervals (CI) of full stack coarse-scale model.

Class	UA	PA	F1	UA CI	PA CI	F1 CI
Gorse	1.00	0.61	0.76	[1.00, 1.00]	[0.31, 0.85]	[0.47, 0.92]
Agricultural land	0.93	0.90	0.90	[0.83, 1.00]	[0.75, 1.00]	[0.81, 0.98]
Bare land	0.92	1.00	0.96	[0.81, 1.00]	[1.00, 1.00]	[0.89, 1.00]
Water	1.00	1.00	1.00	[1.00, 1.00]	[1.00, 1.00]	[1.00, 1.00]
Forest	0.81	0.94	0.87	[0.69, 0.95]	[0.83, 1.00]	[0.78, 0.95]
Grass communities	0.84	0.92	0.88	[0.67, 1.00]	[0.75, 1.00]	[0.73, 1.00]
Overall accuracy	0.89			[0.83, 0.95]		
Kappa	0.86			[0.79, 0.93]		

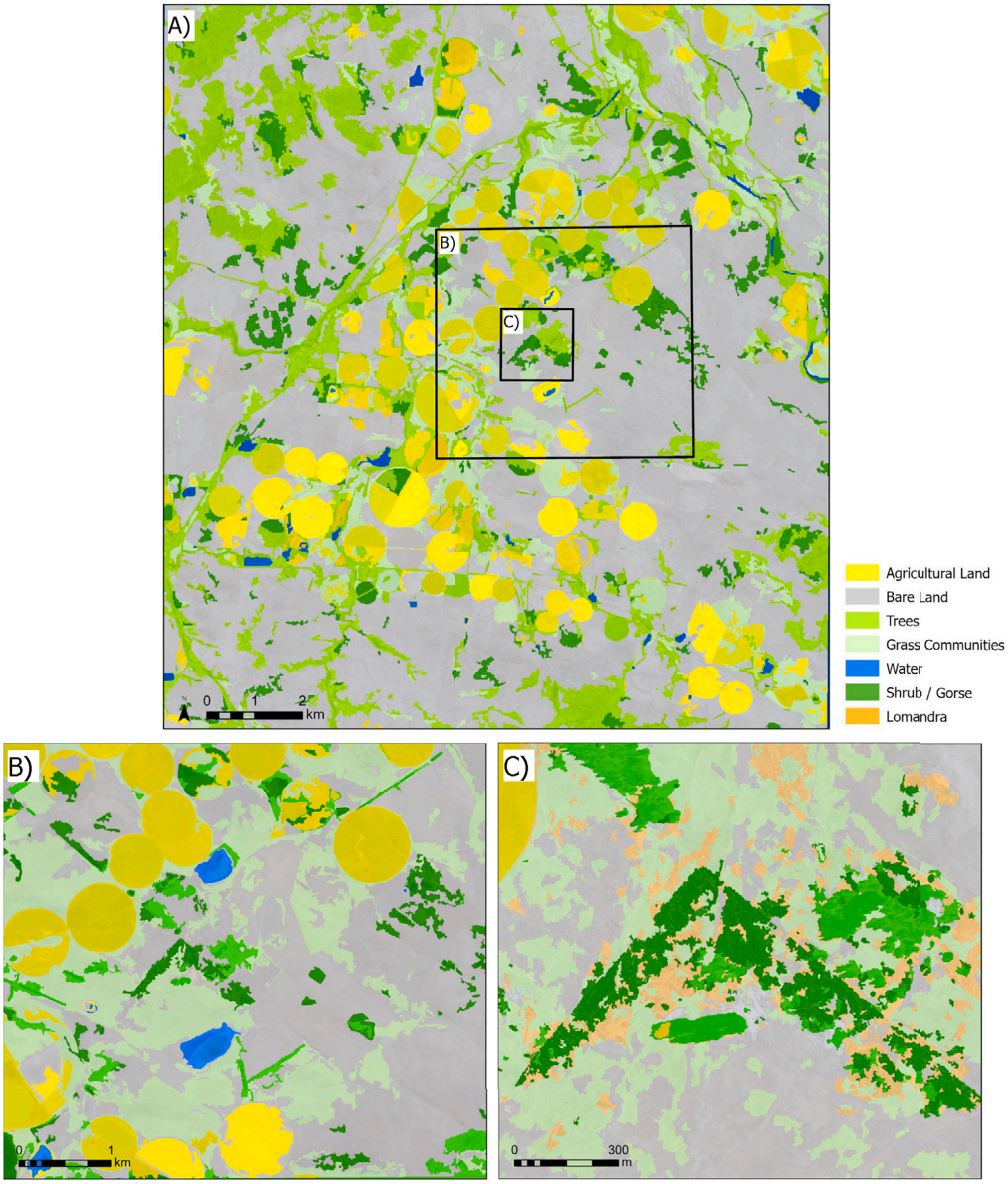

Fig. 8. Best result maps for each resolution scale. (A) Coarse-scale (10 m): Full stack; (B) Mid-scale (3 m): S-2+VI; (C): Fine-scale (0.5 m): Full stack.

References

Agüera, F., Aguilar, F.J., Aguilar, M.A., 2008. Using texture analysis to improve per-pixel classification of very high resolution images for mapping plastic greenhouses. ISPRS J. Photogramm. Remote Sens. 63 (6), 635–646. http://dx.doi.org/10.1016/j.isprsjprs.2008.03.003.

Anderson, S.A.J., Anderson, W.R., 2010. Ignition and fire spread thresholds in gorse (Ulex europaeus). Int. J. Wildland Fire 19 (5), 589–598. http://dx.doi.org/10.1071/WF09008.

Arroyo, L.A., Pascual, C., Manzanera, J.A., 2008. Fire models and methods to map fuel types: The role of remote sensing. Forest Ecol. Manag. 256 (6), 1239–1252. http://dx.doi.org/10.1016/j.foreco.2008.06.048.

Baatz, M., Schäpe, A., 2000. Multiresolution Segmentation – an optimization approach for high quality multi-scale image segmentation. Angew. Geogr. Informationsverarbeitung 12–23.

Bialas, J., Oommen, T., Havens, T.C., 2019. Optimal segmentation of high spatial resolution images for the classification of buildings using random forests. Int. J. Appl. Earth Obs. Geoinf. 82, 101895. http://dx.doi.org/10.1016/j.jag.2019.06.005.

Blaschke, T., 2010. Object based image analysis for remote sensing. ISPRS J. Photogramm. Remote Sens. 65 (1), 2–16. http://dx.doi.org/10.1016/j.isprsjprs.2009.06.004.

Breiman, L., 2001. Random forests. Mach. Learn. 45 (1), 5–32. http://dx.doi.org/10.1023/A:1010933404324.

Congalton, R.G., Green, K., 2008. Assessing the Accuracy of Remotely Sensed Data: Principles and Practices, second ed. CRC Press, Boca Raton, http://dx.doi.org/10.1201/9781420055139.

Cowell, S., Cameron, A., Sprod, D., Appleby, M., 2013. Midlandscapes: Matching actions to opportunities in landscape conservation in the Tasmanian Midlands. In: Linking Australia's Landscapes: Lessons and Opportunities from Large-Scale Conservation Networks. CSIRO Publishing, Collingwood, Victoria, Australia, pp. 85–94.

Dabov, K., Foi, A., Katkovnik, V., Egiazarian, K., 2007. Image denoising by sparse 3-D transform-domain collaborative filtering. IEEE Trans. Image Process. 16 (8), 2080–2095. http://dx.doi.org/10.1109/TIP.2007.901238.

Davidson, N.J., Bailey, T.G., Burgess, S., 2021. Restoring the Midlands of Tasmania: An introduction. Ecol. Manag. Restor. 22 (S2), 3–10. http://dx.doi.org/10.1111/emr.12522.

Department of Natural Resources and Environment Tasmania, 2025. LISTmap. URL: https://maps.thelist.tas.gov.au/listmap/app/list/map.

Dorigo, W., Lucieer, A., Podobnikar, T., Čarni, A., 2012. Mapping invasive Fallopia japonica by combined spectral, spatial, and temporal analysis of digital orthophotos. Int. J. Appl. Earth Obs. Geoinf. 19, 185–195. http://dx.doi.org/10.1016/j.jag.2012.05.004.

Feng, Q., Liu, J., Gong, J., 2015. UAV remote sensing for urban vegetation mapping using random forest and texture analysis. Remote Sens. 7 (1), 1074–1094. http://dx.doi.org/10.3390/rs70101074.

Gillies, S., contributors, 2024. Rasterio. URL: https://github.com/rasterio/rasterio.

Gini, R., Sona, G., Ronchetti, G., Passoni, D., Pinto, L., 2018. Improving tree species classification using UAS multispectral images and texture measures. ISPRS Int. J. Geo-Inf. 7 (8), 315. http://dx.doi.org/10.3390/ijgi7080315.

Guindon, B., Zhang, Y., 2017. Application of the dice coefficient to accuracy assessment of object-based image classification. Can. J. Remote Sens. 43 (1), 48–61. http://dx.doi.org/10.1080/07038992.2017.1259557.

Halgamuge, M.N., Daminda, E., Nirmalathas, A., 2020. Best optimizer selection for predicting bushfire occurrences using deep learning. Nat. Hazards 103 (1), 845–860. http://dx.doi.org/10.1007/s11069-020-04005-3.

Hall-Beyer, M., 2017. Practical guidelines for choosing GLCM textures to use in landscape classification tasks over a range of moderate spatial scales. Int. J. Remote Sens. 38 (5), 1312–1338. http://dx.doi.org/10.1080/01431161.2016.1278314.

Hao, S., Cui, Y., Wang, J., 2021. Segmentation scale effect analysis in the object-oriented method of high-spatial-resolution image classification. Sensors 21 (23), http://dx.doi.org/10.3390/s21237935.

Hartley, R.J.L., Davidson, S.J., Watt, M.S., Massam, P.D., Aguilar-Arguello, S., Melnik, K.O., Pearce, H.G., Clifford, V.R., 2022. A mixed methods approach for fuel characterisation in gorse (Ulex europaeus L.) scrub from high-density UAV laser scanning point clouds and semantic segmentation of UAV imagery. Remote Sens. 14 (19), 4775. http://dx.doi.org/10.3390/rs14194775.

Holtgrave, A.-K., Röder, N., Ackermann, A., Erasmi, S., Kleinschmit, B., 2020. Comparing Sentinel-1 and -2 data and indices for agricultural land use monitoring. Remote Sens. 12 (18), 2919. http://dx.doi.org/10.3390/rs12182919.

Huete, A., 1988. A soil-adjusted vegetation index (SAVI). Remote Sens. Environ. 25 (3), 295–309. http://dx.doi.org/10.1016/0034-4257(88)90106-X.

Hussain, M., Chen, D., Cheng, A., Wei, H., Stanley, D., 2013. Change detection from remotely sensed images: From pixel-based to object-based approaches. ISPRS J. Photogramm. Remote Sens. 80, 91–106. http://dx.doi.org/10.1016/j.isprsjprs.2013.03.006.

Josselin, D., Louvet, R., 2019. Impact of the scale on several metrics used in geographical object-based image analysis: Does GEOBIA mitigate the modifiable areal unit problem (MAUP)? ISPRS Int. J. Geo-Inf. 8 (3), 156. http://dx.doi.org/10.3390/ijgi8030156.

Kavzoglu, T., Tonbul, H., 2018. An experimental comparison of multi-resolution segmentation, SLIC and K-means clustering for object-based classification of VHR imagery. Int. J. Remote Sens. 39 (18), 6020–6036. http://dx.doi.org/10.1080/01431161.2018.1506592.

Kim, Y., van Zyl, J., 2004. Vegetation effects on soil moisture estimation. In: Proc. IEEE Int. Geosci. Remote Sens. Symp.. IGARSS, IEEE, Anchorage, AK, USA, pp. 800–802. http://dx.doi.org/10.1109/IGARSS.2004.1370480.

Lechner, A.M., Stein, A., Jones, S.D., Ferwerda, J.G., 2009. Remote sensing of small and linear features: Quantifying the effects of patch size and length, grid position and detectability on land cover mapping. Remote Sens. Environ. 113 (10), 2194–2204. http://dx.doi.org/10.1016/j.rse.2009.06.002.

Macintyre, P., van Niekerk, A., Mucina, L., 2020. Efficacy of multi-season Sentinel-2 imagery for compositional vegetation classification. Int. J. Appl. Earth Obs. Geoinf. 85, 101980. http://dx.doi.org/10.1016/j.jag.2019.101980.

Marcinkowska-Ochtyra, A., Jarocińska, A., Bzdęga, K., Tokarska-Guzik, B., 2018. Classification of expansive grassland species in different growth stages based on hyperspectral and LiDAR data. Remote Sens. 10 (12), 2019. http://dx.doi.org/10.3390/rs10122019.

McFeeters, S.K., 1996. The use of the Normalized Difference Water Index (NDWI) in the delineation of open water features. Int. J. Remote Sens. 17 (7), 1425–1432. http://dx.doi.org/10.1080/01431169608948714.

Meinel, G., Neubert, M., 2004. A comparison of segmentation programs for high resolution remote sensing data. Int. Arch. Photogramm. Remote Sens. Spat. Inf. Sci. 35.

Menze, B.H., Kelm, B.M., Masuch, R., Himmelreich, U., Bachert, P., Petrich, W., Hamprecht, F.A., 2009. A comparison of random forest and its Gini importance with standard chemometric methods for the feature selection and classification of spectral data. BMC Bioinf. 10, 213. http://dx.doi.org/10.1186/1471-2105-10-213.

Mohammadpour, P., Viegas, D.X., Viegas, C., 2022. Vegetation mapping with random forest using Sentinel 2 and GLCM texture feature—A case study for Lousã Region, Portugal. Remote Sens. 14 (18), 4585. http://dx.doi.org/10.3390/rs14184585.

Niemeyer, I., Marpu, P., Nussbaum, S., 2008. Change detection using object features. In: Blaschke, T., Lang, S., Hay, G. (Eds.), Object-Based Image Analysis. In: Lecture Notes in Geoinformation and Cartography, Springer, Berlin, Heidelberg, pp. 185–201. http://dx.doi.org/10.1007/978-3-540-77058-9_10.

Ogliari, D.G.P., Zanotta, D.C., Fontana, D.C., Bremm, C., Bredemeier, C., Carvalho, P.C.d.F., 2023. Airborne cameras for natural grassland classification in the Pampa biome / Câmeras aerotransportadas para classificação da vegetação em pastagem natural no bioma Pampa. Ciênc. Rural 53 (2), e20210765. http://dx.doi.org/10.1590/0103-8478cr20210765, Open access.

Openshaw, S., 1984. The modifiable areal unit problem. In: Concepts and Techniques in Modern Geography, vol. 38, Geobooks, Norwich, U.K..

Pham, D., Gautam, D., Sheffield, K., 2024. Classifying serrated tussock cover from aerial imagery using RGB bands, RGB indices, and texture features. Remote Sens. 16 (23), 4538. http://dx.doi.org/10.3390/rs16234538.

Plakman, V., Janssen, T., Brouwer, N., Veraverbeke, S., 2020. Mapping species at an individual-tree scale in a temperate forest, using sentinel-2 images, airborne laser scanning data, and random forest classification. Remote Sens. 12 (22), 3710. http://dx.doi.org/10.3390/rs12223710.

Richards, M.A., 2005. Fundamentals of Radar Signal Processing. McGraw-Hill, New York, NY, USA.

Rouse, J.W., Haas, R., Schell, J., Deering, D., 1974. Monitoring vegetation systems in the Great Plains with ERTS. Open J. Ecol. (351), 309.

Sá, A.C.L., Aparicio, B., Benali, A., Bruni, C., Salis, M., Silva, F., Marta-Almeida, M., Pereira, S., Rocha, A., Pereira, J., 2022. Coupling wildfire spread simulations and connectivity analysis for hazard assessment: a case study in Serra da Cabreira, Portugal. Nat. Hazards Earth Syst. Sci. 22 (12), 3917–3938. http://dx.doi.org/10.5194/nhess-22-3917-2022.

scikit-learn developers, 2023. RandomForestClassifier. URL: https://scikit-learn.org/stable/modules/generated/sklearn.ensemble.RandomForestClassifier.html.

Sharples, J.J., Cary, G.J., Fox-Hughes, P., 2016. Natural hazards in Australia: Extreme bushfire. Clim. Change 139, 85–99. http://dx.doi.org/10.1007/s10584-016-1819-3.

Shi, G., Yan, H., Zhang, W., Dodson, J., Heijnis, H., Burrows, M., 2021. Rapid warming has resulted in more wildfires in northeastern Australia. Sci. Total Environ. 771, 144888. http://dx.doi.org/10.1016/j.scitotenv.2020.144888.

Stehman, S.V., Foody, G.M., 2019. Key issues in rigorous accuracy assessment of land cover products. Remote Sens. Environ. 231, 111199. http://dx.doi.org/10.1016/j.rse.2019.05.018.

Taneja, R., Hilton, J., Wallace, L., Reinke, K., Jones, S., 2021. Effect of fuel spatial resolution on predictive wildfire models. Int. J. Wildland Fire 30 (10), 776–789. http://dx.doi.org/10.1071/WF20192.

Taylor, R., Marshall, A.G., Crimp, S., Cary, G.J., Harris, S., 2024. A statistical forecasting model for extremes of the fire behaviour index in Australia. Atmosphere 15 (4), 470. http://dx.doi.org/10.3390/atmos15040470.

Trimble Inc., 2026. eCognition. URL: https://geospatial.trimble.com/products/software/trimble-ecognition.

Trudel, M., Charbonneau, F., Leconte, R., 2012. Using RADARSAT-2 polarimetric and ENVISAT-ASAR dual-polarization data for estimating soil moisture over agricultural fields. Can. J. Remote Sens. 38 (4), 514–527. http://dx.doi.org/10.5589/m12-043.

Tyukavina, A., Stehman, S.V., Foody, G.M., Bontemps, S., See, L., Olofsson, P., Tsendbazar, N.-E., Radoux, J., Komarova, A., Serre, B.M., Song, X.-P., d'Andrimont, R., Koren, G., Potapov, P., Bullock, E.L., Campbell, P., de Bruin, S., Defourny, P., Friedl, M.A., Fritz, S., Hansen, M.C., Herold, M., Lamarche, C., Lesiv, M., Mané, L., Meroni, M., Nickeson, J.E., Pelletier, F., Pickens, A.H., Reiche, J., Schepaschenko, D., Tarrio, K., Verhegghen, A., Woodcock, C.E., Xiao, X., 2025. Land Cover and Change Map Accuracy Assessment and Area Estimation Good Practices Protocol. Version 1.0, Committee on Earth Observation Satellites (CEOS), Working Group on Calibration and Validation (WGCV), Land Product Validation Subgroup, Laxenburg, Austria, http://dx.doi.org/10.5067/DOC/CEOSWGCV/LPV/LC.001.

VirtualTAS, 2025. Capturing futures.

Vizzari, M., 2022. PlanetScope, Sentinel-2, and Sentinel-1 data integration for object-based land cover classification in Google Earth Engine. Remote Sens. 14 (11), 2628. http://dx.doi.org/10.3390/rs14112628.

Xin, Q., Olofsson, P., Zhu, Z., Tan, B., Woodcock, C.E., 2013. Toward near real-time monitoring of forest disturbance by fusion of MODIS and Landsat data. Remote Sens. Environ. 135, 234–247. http://dx.doi.org/10.1016/j.rse.2013.04.002.

Xue, J., Su, B., 2017. Significant remote sensing vegetation indices: A review of developments and applications. J. Sens. 2017, 1–17. http://dx.doi.org/10.1155/2017/1353691.

Yu, P., Zwi, A.B., Zheng, Y., Jia, Y., 2020. Bushfires in Australia: A serious health emergency under climate change. Lancet Planet. Health 4 (1), e7–e8. http://dx.doi.org/10.1016/S2542-5196(19)30267-0.

Zeng, Y., Hao, D., Huete, A., Dechant, B., Berry, J., Chen, J.M., Joiner, J., Frankenberg, C., Bond-Lamberty, B., Ryu, Y., Xiao, J., Asrar, G.R., Chen, M., 2022. Optical vegetation indices for monitoring terrestrial ecosystems globally. Nat. Rev. Earth Environ. 3 (7), 477–493. http://dx.doi.org/10.1038/s43017-022-00298-5.

Zhang, H., Wei, S., Liang, X., Chen, Y., Zhang, H., 2025. Scale effects in mangrove mapping from ultra-high-resolution remote sensing imagery. Int. J. Appl. Earth Obs. Geoinf. 136, 104310. http://dx.doi.org/10.1016/j.jag.2024.104310.